

1  
2  
3  
4  
5  
6  
7  
8  
9  
10  
11  
12  
13  
14  
15  
16  
17  
18  
19  
20  
21  
22  
23  
24  
25  
26  
27  
28  
29  
30  
31  
32  
33  
34  
35  
36  
37  
38  
39  
40  
41  
42  
43  
44  
45  
46  
47  
48  
49  
50  
51  
52  
53  
54  
55  
56  
57  
58  
59  
60

# Tunable Electrical and Thermal Transport in Ice-Templated Multi-Layer Graphene Nanocomposites through Freezing Rate Control

*Scott N. Schiffres<sup>†,1</sup>, Sivasankaran Harish<sup>†,2</sup>, Shigeo Maruyama<sup>2</sup>, Junichiro Shiomi<sup>2</sup>, Jonathan A.*

*Malen<sup>\*,1,3</sup>*

<sup>†</sup> Joint co-authorship; <sup>\*</sup> Corresponding author (jonmalen@andrew.cmu.edu)

<sup>1</sup> Department of Mechanical Engineering, Carnegie Mellon University, 5000 Forbes Ave.,  
Pittsburgh, PA 15213 USA

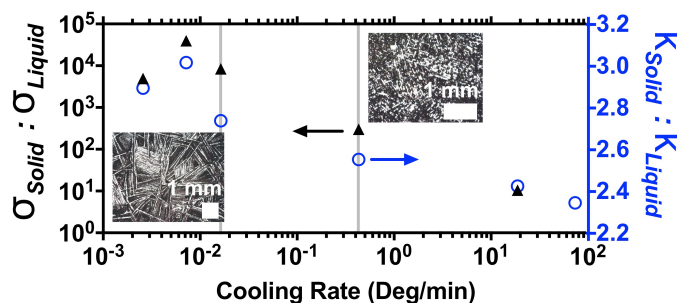
<sup>2</sup> Department of Mechanical Engineering, The University of Tokyo, 7-3-1 Hongo, Bunkyo-ku,  
Tokyo 113-8656, Japan

<sup>3</sup> Department of Material Science & Engineering, Carnegie Mellon University, 5000 Forbes  
Ave., Pittsburgh, PA 15213 USA

KEYWORDS: Phase change nanocomposite, ice-templating, tunable electrical conductivity,  
tunable thermal conductivity, freezing rate dependence, multi-layer graphene, hexadecane

**Abstract.** We demonstrate tunable electrical and thermal conductivities through freezing rate control in solution-based nanocomposites. For a prototypical suspension of 1 vol % multi-layer graphene suspended in hexadecane, the solid-liquid electrical conductivity contrast ratio can be tuned from one to four-and-a-half orders of magnitude for freezing rates between  $10^2$  °C/min to  $10^{-3}$  °C/min. We hypothesize that this dramatic variation stems from ice-templating, whereby crystal growth drives nanoparticles into concentrated inter-crystal regions, increasing the percolation pathways and reducing the inter-nanoparticle electrical resistance. Optical microscopy supports the ice-templating hypothesis, as these dramatic property changes coincide with changing crystal size. Under the same range of freezing rates, the nanocomposite solid-liquid thermal conductivity contrast ratio varies between 2.3 and 3.0, while pure hexadecane's varies between 2.1 and 2.6. The nanocomposite's thermal conductivity contrast ratios and solid phase enhancements are greater than effective medium theory predictions. We suggest this is due to ice-templating, consistent with our electrical measurements, as well as nanoparticle induced molecular alignment of alkanes.

### Table of Contents Graphic.



**Main Text.**

1  
2  
3  
4  
5  
6 Solution-based nanoparticle composite materials promise scalability for diverse energy  
7  
8 technologies, yet challenges persist in the control of nanoparticle network morphology, as well  
9  
10 as the resulting electrical and thermal conductivities. Morphological control of these transport  
11  
12 properties has scientific and technological importance, with applications to electrical energy  
13  
14 storage,<sup>1-3</sup> thermal energy storage,<sup>4-13</sup> and composite materials.<sup>14-21</sup> Ice-templated materials are  
15  
16 freeze-cast composites that possess intricate structures on multiple length scales – ranging from  
17  
18 nanometers to millimeters.<sup>22</sup> These multiple length scales emerge when the base fluid solidifies  
19  
20 into snowflake-like crystals, driving or “templating” the nanoparticles into the inter-crystal  
21  
22 region.<sup>22</sup> For example, ice-templated bio-mimetic seashell nacre is reported to have enhanced  
23  
24 mechanical properties derived from the intricate micro-structuring, but the effect of ice-  
25  
26 templating on electrical and thermal properties remains unexplored.  
27  
28  
29  
30  
31  
32  
33

34  
35 Controllable transport properties in phase change nanocomposites can benefit applications in  
36  
37 thermal and electrical energy storage. Phase change thermal storage seeks to reduce building  
38  
39 heating and cooling energy consumption by moderating temperature swings and compensating  
40  
41 for temporal offsets in energy supply and demand.<sup>6</sup> Thermal energy storage is also an appealing  
42  
43 way to cool power electronics during peak loads,<sup>7,8</sup> and to store off-peak thermal energy in  
44  
45 industrial processes.<sup>9-11,23,24</sup> In melting or freezing, the thermal energy storage rate is proportional  
46  
47 to the phase change material’s thermal conductivity.<sup>4</sup> Room-temperature phase change materials,  
48  
49 like alkanes, possess poor thermal conductivity which limits the energy storage and withdrawal  
50  
51 rate. This has led to interest in increasing the thermal conductivity of phase-change materials  
52  
53 through the addition of high thermal conductivity nanoparticles.<sup>5,12,13</sup> Tunable properties through  
54  
55  
56  
57  
58  
59  
60

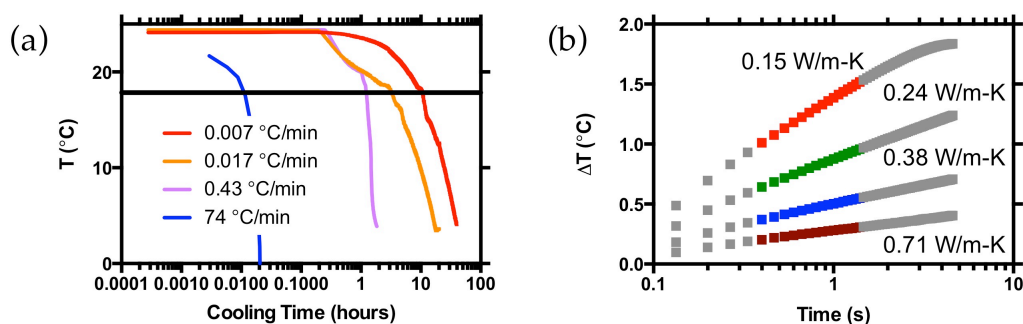
1  
2  
3 phase change could also optimize electrical energy storage through the control of nanoparticle  
4 network morphology, and electrical conductivity.<sup>1</sup>  
5  
6  
7  
8  
9

10 Recently, molecular dynamics simulations have predicted that the presence of carbon  
11 nanotubes (CNTs) and graphene induce a more orderly alkane crystallization, thereby increasing  
12 the thermal conductivity of phase change nanocomposites.<sup>25-27</sup> Order induced near the  
13 nanoparticle surface is also reported to reduce the time for crystals to nucleate.<sup>14</sup> Simulations of  
14 Babaei *et al.*<sup>27</sup> show that introducing CNTs and graphene to liquid alkane enhances the solid-  
15 state thermal conductivity of the alkane significantly compared to its liquid state. This  
16 mechanism has been proposed to explain the unexpectedly large solid-liquid thermal  
17 conductivity enhancements recently reported using graphite-hexadecane,<sup>4</sup> CNT-octadecane,<sup>11</sup>  
18 and CNT-hexadecane suspensions.<sup>9</sup> However, the mechanisms responsible for these unusual  
19 solid-liquid thermal conductivity enhancements remains unclear, and its dependence on freezing  
20 rate is as yet unknown.  
21  
22  
23  
24  
25  
26  
27  
28  
29  
30  
31  
32  
33  
34  
35  
36  
37  
38

39 Hence, we seek to understand the electrical and thermal transport properties of phase change  
40 nanocomposites by varying the underlying microstructure through the freezing rate. Using  
41 multi-layer graphene (MLG) nanoplatelet-hexadecane suspensions, we show that slower freezing  
42 rates lead to nanocomposites with improved electrical and thermal conductivities. Surprisingly,  
43 the electrical conductivity contrast ratio  $\sigma_{Solid}/\sigma_{Liquid}$  can be tuned between one and four-and-a-  
44 half orders of magnitude, and the solid-liquid thermal conductivity contrast ratio  $k_{Solid}/k_{Liquid}$   
45 can be tuned between 2.3-3.0 by varying only the freezing rate.  
46  
47  
48  
49  
50  
51  
52  
53  
54  
55  
56  
57  
58  
59  
60

## Results and Discussion

Samples were frozen at rates between  $10^{-3}$  °C/min and  $10^2$  °C/min (Figure 1a) using Peltier and liquid nitrogen cooling. Temperature, thermal conductivity, and electrical conductivity were measured every minute during freezing. Representative transient hot wire thermal conductivity measurements of temperature rise versus time are shown in Figure 1b. Instrumentation and data analysis are further described in the Materials and Methods section. The solid-liquid contrast ratios of electrical and thermal conductivity for hexadecane with 1 vol % MLG nanoplatelets are shown in Figure 2a and 2b where liquid properties are at 24 °C and solid properties are at 5 °C (non-normalized electrical conductivity measurements are plotted in Supplementary Information Figure S1). The liquid state has an average electrical conductivity of  $0.02 \mu\text{S/cm}$  (ranging from 0.006 to  $0.06 \mu\text{S/cm}$ ) at 24 °C. The minimum  $\sigma_{\text{Solid}}/\sigma_{\text{Liquid}}$  of just one order-of-magnitude was achieved at the rapid cooling rate of 19 °C/min, and surged to four-and-a-half orders-of-magnitude at the minimum tested cooling rate of  $10^{-3}$  °C/min. The  $\sigma_{\text{Solid}}/\sigma_{\text{Liquid}}$  ratios are greater than reported by Zheng *et al.*, where the  $\sigma_{\text{Solid}}/\sigma_{\text{Liquid}}$  ranged from 50 to 250 times for 0.2 to 1.0 vol % graphite-hexadecane suspensions. Similar  $\sigma_{\text{Solid}}/\sigma_{\text{Liquid}}$  ratios were observed by Sun *et al.* in anti-agglomeration functionalized CNT, while much lower  $\sigma_{\text{Solid}}/\sigma_{\text{Liquid}}$  ratios were observed in non-functionalized CNT suspensions (Figure 2a).<sup>4,9</sup>



1  
2  
3  
4  
5  
6  
7  
8  
9  
10  
11  
12  
13  
14  
15  
16  
17  
18  
19  
20  
21  
22  
23  
24  
25  
26  
27  
28  
29  
30  
31  
32  
33  
34  
35  
36  
37  
38  
39  
40  
41  
42  
43  
44  
45  
46  
47  
48  
49  
50  
51  
52  
53  
54  
55  
56  
57  
58  
59  
60

Figure 1. a) Representative plots of sample cooling versus time on a logarithmic scale. The fastest freezing (blue) was liquid nitrogen cooled, while others were frozen with a Peltier cooler. The black line is the phase transition temperature for bulk hexadecane of 17.8 °C. b) Typical transient hot wire thermal conductivity measurement data. The colored region of each line represents the segment of the transient hot wire data used to determine the thermal conductivity. The red, green, blue and brown data points are for liquid hexadecane, liquid nanocomposite, solid hexadecane, and solid nanocomposite, respectively.

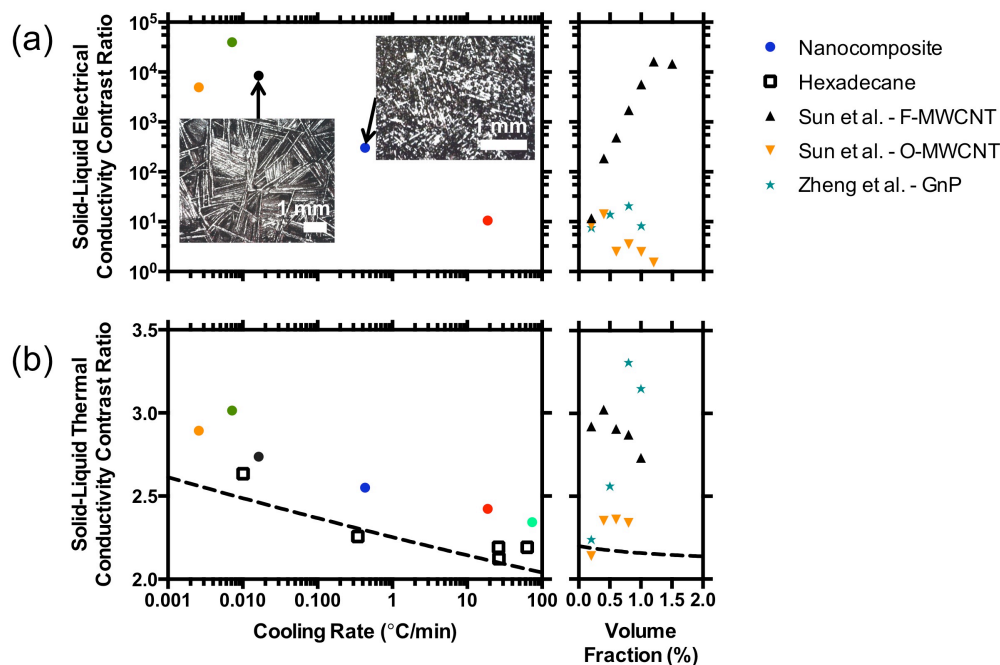


Figure 2. a) The solid-liquid electrical conductivity contrast ratios ( $\sigma_{Solid}/\sigma_{Liquid}$ ) are plotted versus cooling rate for the hexadecane with 1 vol % MLG. The mean liquid state electrical conductivity is 0.02  $\mu\text{S}/\text{cm}$  at 24 °C. Solid measurements were taken at 5 °C. Inset images

1  
2  
3 of the top surface of the nanocomposite were taken with an optical microscope at the  
4  
5  
6 respective cooling rates. The length dependence of crystals with cooling rate is notable. To  
7  
8 to the right are the solid-liquid electrical contrast ratios achieved by Sun *et al.*, and Zheng *et*  
9  
10 *al.* versus volume fraction, as freezing rate was not reported. Sun *et al.* measured  
11  
12 suspensions of pristine and anti-agglomeration functionalized multi-walled carbon  
13  
14 nanotubes (O-MWCNT and F-MWCNTs) in hexadecane, while Zheng *et al.* measured  
15  
16 graphite nanoplatelets (GnP) in hexadecane. b) The solid-liquid thermal conductivity  
17  
18 contrast ratios ( $k_{Solid}/k_{Liquid}$ ) are plotted versus cooling rate for bulk hexadecane (black  
19  
20 squares) and for hexadecane with 1 vol % MLG (circles color coded by cooling rate). The  
21  
22 average liquid state thermal conductivity of the liquid nanocomposite and hexadecane are  
23  
24 0.24 W/m-K and 0.15 W/m-K at 24 °C. The right plot shows the solid-liquid thermal  
25  
26 conductivity contrast ratios of Sun *et al.*, and Zheng *et al.* versus vol %. The dashed lines  
27  
28 are the Nan *et al.* effective medium predicted contrast ratios (details are in the Methods  
29  
30 and Materials section).  
31  
32  
33  
34  
35  
36  
37  
38  
39

40 Liquid hexadecane with 1 vol % MLG nanoplatelets has a thermal conductivity at 24 °C of  
41  
42 0.24 W/m-K, which is 65% greater than liquid hexadecane. The nanocomposite solid-liquid  
43  
44 thermal conductivity contrast ratio  $k_{Solid}/k_{Liquid}$  can be controlled from 2.3 to 3.0 for freezing  
45  
46 rates between  $10^2$  °C/min to  $10^{-3}$  °C/min, as shown in Figure 2b (non-normalized thermal  
47  
48 conductivity measurements are plotted in Supplementary Information Figure S2). For the same  
49  
50 range of freezing rates, pure hexadecane  $k_{Solid}/k_{Liquid}$  ratio followed a similar trend and varied  
51  
52 from 2.1 to 2.6. Our maximum  $k_{Solid}/k_{Liquid}$  ratio of 3.0 is near to Zheng *et al.*'s published  
53  
54  
55  
56  
57  
58  
59  
60

1  
2  
3  
4  $k_{Solid}/k_{Liquid}$  ratio for 1 vol % graphite nanoplatelets in hexadecane.<sup>4</sup> The nanocomposite  
5  
6 thermal conductivity enhancement relative to similarly frozen pure hexadecane  $k_{NC} / k_{Base}$  is  
7  
8 1.81±0.08 over the range of freezing rates, while the nanocomposite liquid precursor suspension  
9  
10 relative to pure liquid hexadecane  $k_{NC} / k_{Base}$  is 1.65±0.07.  
11  
12  
13  
14  
15

16 Paralleling these changes in electrical and thermal conductivity, the nanocomposite develops  
17  
18 longer and thicker needle-like patterns with slower freezing, as shown in insets of Figure 2a. In  
19  
20 a process analogous to the ice-templating of a bio-mimetic seashell, we observe a micro-  
21  
22 structural change in the nanocomposite with freezing rate.<sup>22</sup> These images reveal that the  
23  
24 nanocomposite solidifies through needle-like crystals that are mostly aligned parallel to  
25  
26 neighboring needles. Environmental scanning electron microscopy (ESEM) images recorded at  
27  
28 0.5 °C/min reveal the presence of needle-like structures that vanish upon melting  
29  
30 (Supplementary Information Figure S3). Due to experimental constraints, slower cooled ESEM  
31  
32 studies could not be performed.  
33  
34  
35  
36  
37  
38  
39

40 Measurements of electrical and thermal conductivities through freezing reveal an exponential  
41  
42 increase in electrical conductivity for a linear increase in thermal conductivity (Figure 3a). A  
43  
44 common trend emerges for electrical versus thermal conductivity when various cooling rates are  
45  
46 plotted together (Figure 3b). Moderately and slowly cooled samples differ only in the extent of  
47  
48 their thermal and electrical conductivity enhancements, not in the path. Contrastingly, samples  
49  
50 frozen more rapidly with liquid nitrogen measure a significantly smaller improvement in both  
51  
52 electrical and thermal conductivity through freezing.  
53  
54  
55  
56  
57  
58  
59  
60



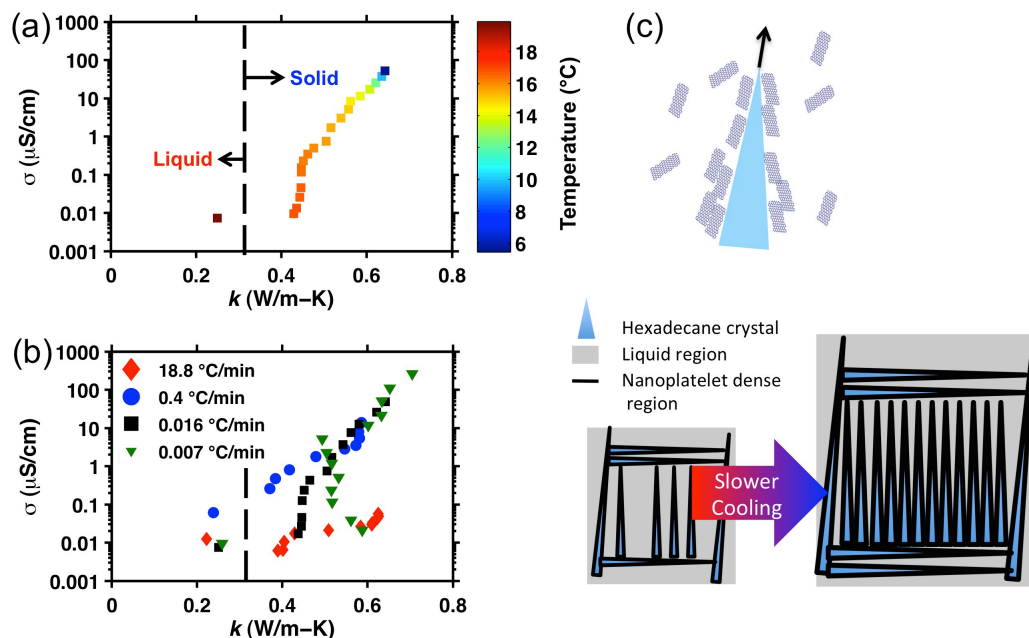


**Figure 3.** a) Plots the electrical versus thermal conductivity during a freezing at  $0.016\text{ }^\circ\text{C}/\text{min}$  with each datapoints color representing the temperature at that measurement. After freezing there is an exponential increase in electrical conductivity for a linear change in thermal conductivity. b) The trends for electrical versus thermal conductivity taken at various cooling rates show a similar trend except for the rapid liquid nitrogen cooled data ( $19\text{ }^\circ\text{C}/\text{min}$ ). The trend shared by the slowest and moderate cooling rates differ primarily in the final extent of enhancement but not in the path to that enhancement versus temperature. The liquid nitrogen cooled sample ( $19\text{ }^\circ\text{C}/\text{min}$ ) does not follow this trend, and has less improvement in both electrical and thermal conductivity than the slower cooled measurements. c) This graphic illustrates our hypothesis that crystal growth drives MLG nanoplatolets to grain boundary, and that slower freezing will lead to larger hexadecane crystal growth. We suggest that ice-templating leads to increased electrical percolation pathways and reduced electrical resistance between nanoplatolets, as well as reduced inter-nanoparticle thermal resistance.

1  
2  
3  
4  
5  
6 Drawing from related research on particle incorporation during metal solidification, the  
7  
8 underlying mechanism that propels nanoparticles out of the crystallizing hexadecane is the  
9  
10 reduced surface energy of the nanoparticles in the liquid versus the solid phase (Figure 3c).<sup>28</sup>  
11  
12 This surface energy difference provides the propulsive force pushing the nanoparticles away  
13  
14 from the solidification front, but is countered by the viscous drag acting on the nanoparticles  
15  
16 traveling through the melt.<sup>28</sup> If the freezing front is moving beyond a critical speed, the drag  
17  
18 acting on a nanoparticle will exceed the free-energy gradient driving force, leaving the  
19  
20 nanoparticles engulfed in the crystal, rather than concentrated and compressed into the inter-  
21  
22 crystal region. Larger crystals grown at slower cooling rates will have more nanoparticles  
23  
24 accumulated at the inter-crystal region, as illustrated in Figure 3c. We hypothesize that the  
25  
26 nanoparticle rich inter-crystal region creates additional percolation pathways for electrical  
27  
28 conduction and reduced inter-nanoparticle electrical resistance. The analysis that follows  
29  
30 suggests that electrical conductivity is highly sensitive to the morphology of the nanoparticle rich  
31  
32 regions due to percolation and the inter-nanoparticle tunneling separation, while thermal  
33  
34 conductivity is approximately a linear function of the constituent properties. It follows that the  
35  
36 exponential enhancement of electrical conductivity with linear enhancement of thermal  
37  
38 conductivity is consistent with crystal growth ice-templating the nanoparticle network concurrent  
39  
40 with shifting constituent properties through solidification.  
41  
42  
43  
44  
45  
46  
47  
48  
49  
50

51 The freezing rate controlled solid-liquid electrical conductivity ratio can be analyzed through  
52  
53 percolation theory. Percolation theory for electrical conductivity due to a conductive  
54  
55 nanoparticle in an insulating base material is often modeled as,  
56  
57  
58  
59  
60

$$\sigma \propto \left( \frac{\phi - \phi_C}{1 - \phi_C} \right)^U, \quad (1)$$

where  $\phi_C$  is the critical nanoparticle volume fraction threshold, and  $U$  is the universal critical exponent. The electrical conductivity contrast ratio predicted from densification of nanoparticles is

$$\frac{\sigma_{Solid}}{\sigma_{Liquid}} \propto \left( \frac{\phi' - \phi_C}{1 - \phi_C} \right)^U \left( \frac{\phi - \phi_C}{1 - \phi_C} \right)^{-U} \left( \frac{\phi}{\phi'} \right), \quad (2)$$

where  $\phi'$  is the volume fraction in the inter-crystal high concentration regions.

Using typical values for MLG nanoplatelets'  $\phi_C$  and  $U$  of 0.05-0.1% and 2-3, respectively, the crystals would have to concentrate the nanoplatelets to a volume fraction of greater than 30% to have a solid-liquid electrical conductivity contrast ratio of four-and-a-half orders of magnitude.<sup>4,29</sup> This densification theory is also supported by Sun *et al.*'s finding that anti-agglomeration functionalized multi-walled CNT-hexadecane nanocomposites have much greater solid-liquid contrast ratios than pristine multi-walled CNT-hexadecane nanocomposites that more readily agglomerate in the liquid state (Figure 2a).<sup>9</sup>

Because the hexadecane is electrically insulating, the nanocomposite electrical conductivity is a function of the inter-nanoplatelet electrical resistance, the nanoplatelet conductance, and the nanoplatelet network morphology. The nanoplatelets' high electrical conductance suggests that the electrical resistance of the inter-nanoparticle junctions will dominate the nanocomposite's electrical properties.<sup>19</sup> The resistance of a tunneling junction increases exponentially with the junction separation ( $R_{Elec} \propto R_0 e^{\beta d}$ ). Rampi *et al.* considered the electrical resistance through various length alkane chains with different end-groups (alkane-thiols, alkane-phenols, etc.).<sup>30</sup>

1  
2  
3 While the alkane chemistry characteristic tunneling length,  $1/\beta$ , depends on end-group chemistry,  
4 the range of characteristic lengths stays within a band of 1.15 to 1.64 Å.<sup>30</sup> Under the assumption  
5 that the inter-nanoparticle junctions in the percolating network obey similar tunneling behavior,  
6 our electrical conductivity enhancement from one to four-and-a-half orders of magnitude can be  
7 explained by a reduction in the inter-nanoparticle separation of ~1 nm between different freezing  
8 rates.  
9  
10  
11  
12  
13  
14  
15  
16  
17  
18  
19

20 Effective medium theory (EMT) is used to predict the thermal conductivity of composite  
21 materials based on the thermal conductivities and volume fractions of the continuous base phase  
22 and the discontinuous inclusion phase, the thermal boundary conductance, as well as the  
23 dimensions and orientation of the inclusions.<sup>31–34</sup> We employed the Nan *et al.* model for  
24 randomly oriented ellipsoidal particles, which is further described in the Materials and Methods  
25 section.<sup>32</sup>  
26  
27  
28  
29  
30  
31  
32  
33  
34  
35

36 Our  $k_{Solid}/k_{Liquid}$  ratios versus cooling rate exceed the EMT predictions, shown as dashed lines in  
37 Figure 2b. The  $k_{Solid}/k_{Liquid}$  ratios of Sun *et al.* and Zheng *et al.* also exceed these predictions. As a  
38 different perspective, Figure 4 compares the experimental and EMT predicted thermal  
39 conductivity enhancement ratios  $k_{NC}/k_{Base}$  as a function of base hexadecane thermal conductivity  
40  $k_{Base}$ . EMT predicts that  $k_{NC}/k_{Base}$  will decrease through freezing because the  $k_{Base}$  increases,  
41 therefore reducing the impact of higher thermal conductivity nanoparticles. EMT correctly  
42 captures ~80% of the enhancement as being the result of increased base thermal conductivity,  
43 which is also evident from the identical hexadecane and nanocomposite  $k_{Solid}/k_{Liquid}$  trends in  
44  
45  
46  
47  
48  
49  
50  
51  
52  
53  
54  
55  
56  
57  
58  
59  
60

Figure 2b. Nonetheless, the remaining  $\sim 20\%$ , visualized as the offset of solid data from EMT predictions for randomly oriented ellipsoidal nanoplatelets in Figure 4, is unaccounted by EMT.

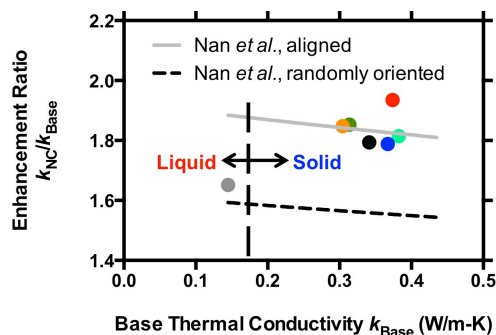


Figure 4. Shows the liquid and solid nanocomposite thermal conductivity enhancements versus base material thermal conductivity. The dashed black line is an effective medium prediction of how enhancement should change versus base thermal conductivity. We used the Nan *et al.* model for oblate ellipsoidal nanoparticles with random (dashed line) and fully aligned (grey line) orientations, with details on the EMT model in Materials and Methods.

The failure of EMT suggests that the assumptions of the model are not valid through phase change. One possible contributing factor is that graphite nanoplatelets actually increase the thermal conductivity of the surrounding base material, thus making the  $k_{Solid}/k_{Liquid}$  ratio appear larger. The molecular dynamics simulations of Babaei *et al.* predict that the presence of graphitic nanoparticles in an octadecane base increases the molecular alignment parameter from 0.15 to 0.91. Babaei *et al.* noted that this alignment parameter in turn has a strong effect on thermal conductivity, with octadecane solid thermal conductivity varying from 0.30 W/m-K to 1.13 W/m-K for alignment parameters between 0.15 and 0.99.<sup>27</sup> A second factor is that the nanoparticle network experiences a morphological change due to ice-templating that puts the

1  
2  
3 nanoparticles into better contact and reduced separation through nanoplatelet alignment. The  
4 potential increase due to alignment of the MLG nanoplatelets is quantified by the Nan *et al.*  
5 model, and the prediction shown in Figure 4 is in reasonable agreement with data. While  
6 electrical conductivity is extremely sensitive to the freezing rate due to ice-templating, the  
7 thermal conductivity is less sensitive as  $k_{NC}/k_{Base}$  of solid samples does not have a clear trend  
8 versus cooling rate (Figure 4).  
9  
10  
11  
12  
13  
14  
15  
16  
17  
18  
19

20 To conclude, this study of MLG nanoplatelet nanocomposites has observed that electrical  
21 conductivity, thermal conductivity and ice-templating micro-structure are tunable through the  
22 freezing rate. The nanocomposite has a tunable  $\sigma_{Solid}/\sigma_{Liquid}$  ratio that spans over four orders-  
23 of-magnitude with the freezing rate, that we hypothesize is caused by ice-templating, whereby  
24 nanoplatelets are driven away from the solid-liquid interface and concentrated in the inter-crystal  
25 regions. The variation of the thermal conductivity with freezing rate cannot be fully explained  
26 by the hexadecane freezing rate dependence, as the nanocomposite thermal conductivity contrast  
27 ratio and solid phase enhancement follow trends contrary to effective medium theory. We  
28 suggest this additional enhancement through freezing is due to ice-templating, consistent with  
29 our electrical measurements, as well as nanoparticle induced molecular alignment of hexadecane.  
30  
31  
32  
33  
34  
35  
36  
37  
38  
39  
40  
41  
42  
43  
44  
45

## 46 **Materials and Methods.**

47  
48 **Sample Preparation.** All liquid nanoparticle suspensions and nanocomposite measurements  
49 were performed on freshly prepared mixtures of hexadecane and MLG nanoplatelets. Liquid  
50 phase exfoliated MLG nanoplatelets (XG Science XGnP-25) were exposed to an ultraviolet light  
51 source (Spectroline Model XX-15A UV 365 nm with two BLE-1800B lamps) for 20 minutes and  
52  
53  
54  
55  
56  
57  
58  
59  
60

1  
2  
3 were then dispersed into hexadecane at 1 vol % in 10mL batches (the Raman spectra before and  
4 after UV exposure is in Supplementary Information Figure S4). Sonication was performed with  
5 a Fischer Scientific 550 tip sonicator with a 1/8" microtip at an amplitude setting of 2 for 60  
6 minutes. After sonication the average nanoplatelet dimensions were 1-2  $\mu\text{m}$  diameter and 4-10  
7 nm thickness, as verified by atomic force microscopy and transmission electron microscopy  
8 (Supplementary Information Figure S5).  
9  
10  
11  
12  
13  
14  
15  
16  
17  
18  
19

20 **Freezing Method.** The nanocomposites were frozen and tested in an acrylic channel with  
21 built-in electrical conductivity and thermal conductivity probes (shown in the Supplementary  
22 Information S6). The bottom of the acrylic holder is 300  $\mu\text{m}$  thick and was placed into direct  
23 contact with a Peltier cooler or a liquid nitrogen bath (for the highest freezing rates).  
24 Nanocomposite and pure hexadecane samples were cooled from room temperature (24  $^{\circ}\text{C}$ ) with  
25 a Peltier cooler at rates between 0.003  $^{\circ}\text{C}/\text{min}$  and 0.4  $^{\circ}\text{C}/\text{min}$ , or with a liquid nitrogen bath  
26 between 19  $^{\circ}\text{C}/\text{min}$  and 74  $^{\circ}\text{C}/\text{min}$  (Figure 1a). The fastest cooling (74  $^{\circ}\text{C}/\text{min}$ ) was performed  
27 with the liquid nanocomposite in an aluminum channel that precluded electrical conductivity  
28 measurement. These freezing rates are based on the slope of the temperature decrease with time,  
29 about a 3  $^{\circ}\text{C}$  window centered at the freezing point of hexadecane (17.8  $^{\circ}\text{C}$ ).  
30  
31  
32  
33  
34  
35  
36  
37  
38  
39  
40  
41  
42  
43  
44  
45

46 **Electrical and Thermal Conductivity Measurements.** Electrical conductivity ( $\sigma$ ) is  
47 measured between two aluminum plates on opposite sidewalls of the vessel. The conductance is  
48 solved for in this simple geometry by  $\sigma = \frac{L}{RA}$ , where  $L$  is the separation between the parallel  
49 plates and  $A$  is the wetted surface area of the parallel plates. MATLAB software coordinated the  
50 control of the Peltier device, and measurements of the electrical and thermal conductivity.  
51  
52  
53  
54  
55  
56  
57  
58  
59  
60

1  
2  
3  
4  
5  
6 Thermal conductivity was measured with a transient hot wire that was initially benchmarked  
7  
8 with measurements of liquid water and glycerol.<sup>35</sup> Transient hot wire involves Joule heating a  
9  
10 thin platinum wire with a Heavyside function, and measuring the wire's resulting temperature  
11  
12 rise as a function of time. The wire temperature is sensed through the wire's temperature  
13  
14 dependence of electrical resistance, *i.e.*, the thermoresistance. The thermal conductivity of the  
15  
16 surrounding medium dictates the wire's temperature rise, and is accurately described by an  
17  
18 analytical solution to the heat diffusion equation for line heating of an infinite medium. This  
19  
20 solution can be manipulated to isolate thermal conductivity  $k$  in terms of the volumetric heating  
21  
22 per length of wire  $q$ , and the rate of temperature rise  $\Delta T$  versus the natural log of time  $\ln t$  since  
23  
24 the beginning of the Heavyside function,<sup>35</sup>  
25  
26  
27  
28

$$k = \frac{q/4\pi}{d\Delta T/d\ln t} \quad (3)$$

29  
30  
31  
32

33 To extract thermal conductivity, we determine  $d\Delta T/d\ln t$  from experimental data, as shown in  
34  
35 Figure 1b. As is typically done with transient hotwire, we use a truncated data set spanning the  
36  
37 time range of 0.4 s to 1.5 s as marked in Figure 1b. At lesser times the heat capacity of the  
38  
39 metal wire itself may influence  $\Delta T$ , while at greater times the thermal response may be  
40  
41 influenced by the vessel boundaries or natural convection. We note that the thermal penetration  
42  
43 depth ( $\sqrt{4kt/C}$ , where  $C$  is the volumetric heat capacity) at 1.5 s is only 1.2 mm for the highest  
44  
45  $k$  sample, while the distance from the wire to the vessel floor is much greater (4 mm).  
46  
47  
48  
49  
50  
51  
52

53 Our implementation of this technique uses a 25.4  $\mu\text{m}$  diameter Platinum wire of length 40 mm  
54  
55 coated in a 2.0  $\mu\text{m}$  Isonel insulation coating (A-M Systems). The current Heavyside function is  
56  
57  
58  
59  
60



delivered by the source-side of the Sourcemeter 2400, which joule heats the wire. Simultaneously, the Sourcemeter 2400 sense-side directly measures the voltage across the wire versus time. Uncertainties in the measurements were based on observed variability between samples and measurements, as well as systematic uncertainties used in the input parameters (i.e., resistance, thermoresistance, wire diameter, wetted area) used to infer the values of electrical and thermal conductivity from the experiments. The uncertainty is 10% for the electrical conductivity, and 2% for the thermal conductivity.

**Effective Medium Theory.** We compare our results to the EMT model proposed by Nan *et al.* for oriented oblate ellipsoidal particles:<sup>32</sup>

$$\frac{k_{NC}}{k_{Base}} = \frac{2 + \phi \left[ \beta_{11}(1 - L_{11}) \left( 1 + \langle \cos^2 \theta \rangle \right) + \beta_{33}(1 - L_{33}) \left( 1 - \langle \cos^2 \theta \rangle \right) \right]}{2 - \phi \left[ \beta_{11} L_{11} \left( 1 + \langle \cos^2 \theta \rangle \right) + \beta_{33} L_{33} \left( 1 - \langle \cos^2 \theta \rangle \right) \right]}, \quad (4)$$

where  $k_{NC}$  is the nanocomposite thermal conductivity,  $k_{Base}$  is the base matrix thermal conductivity,  $k_{NP}$  is the nanoparticle thermal conductivity,  $\phi$  is the MLG volume fraction,

$$L_{11} = \frac{p^2}{2(p^2 - 1)} + \frac{p}{2(1 - p^2)^{3/2}} \cos^{-1} p, \quad L_{33} = 1 - 2L_{11}, \quad p \text{ is the aspect ratio of the thickness to}$$

$$\text{length} \quad p = a_3/a_1, \quad \beta_{ii} = \left( k_{ii}^C - k_{Base} \right) / \left( k_{Base} + L_{ii} \left( k_{ii}^C - k_{Base} \right) \right),$$

$$\langle \cos^2 \theta \rangle = \left( \int \rho(\theta) \cos^2 \theta \sin \theta d\theta \right) / \left( \int \sin \theta d\theta \right), \quad k_{ii}^C = k_{NP} / \left( 1 + (1 + 2p) \left( \frac{1}{h_{TBC} a_3} \right) L_{ii} k_{NP} \right), \text{ and } h_{TBC} \text{ is}$$

the thermal boundary conductance. The model shown in Figures 2b and 4 assume a nanoparticle that is 1  $\mu\text{m}$  x 7nm at 1 vol % with  $k_{NP}$  is 300 W/m-K, and an assumed thermal boundary conductance  $h_{TBC}$  is 12 MW/m<sup>2</sup>-K based on the experimentally measured interface between

1  
2  
3 carbon nanotubes and water.<sup>36</sup> We note, the results here are insensitive to the value of  $h_{\text{TBC}}$  in the  
4  
5 range predicted by simulations of various graphene and CNT nanocomposites.<sup>36-38</sup>  
6  
7  
8  
9

10  
11 **Acknowledgement/Funding Sources.** This material is based upon work supported by the  
12 National Science Foundation under Grant No. 1209752, the Japanese Society for the Promotion  
13 of Science Summer Institute 2012, the AFOSR YIP FA9550-11-1-0030, and the Japanese  
14 Government Monbukagakusho (MEXT) Scholarship for S.H. Acknowledgment is made to the  
15 donors of the American Chemical Society Petroleum Research Fund for partial support of this  
16 research PRF51423DN10. A part of this work was conducted in the Research Hub for Advanced  
17 Nano Characterization, The University of Tokyo, supported by the Ministry of Education,  
18 Culture, Sports, Science and Technology, Japan. We would also like to acknowledge useful  
19 discussions with C. Pistorius, A. J.H. McGaughey, and Y. Rabin.  
20  
21  
22  
23  
24  
25  
26  
27  
28  
29  
30  
31  
32

33 **Abbreviations.** CNT, carbon nanotube; MLG, multi-layer graphene; ESEM, environmental  
34 scanning electron microscopy; EMT, effective medium theory.  
35  
36  
37  
38

39 **Supporting Information Available.**

40  
41  
42 Plot of nanocomposite and hexadecane thermal conductivity versus cooling rate; Plot of  
43 nanocomposite electrical conductivity versus cooling rate; Environmental scanning electron  
44 microscopy of the nanocomposite; Raman spectra of pristine and UV exposed MLG  
45 nanoplatelets; Scanning electron microscopy image of pre-sonicated graphite MLG nanoplatelets  
46 and tunneling electron microscopy image of post-sonicated MLG nanoplatelets; Schematic and  
47 picture of the experimental setup. This material is available free of charge via the Internet at  
48  
49  
50  
51  
52  
53  
54  
55  
56  
57  
58  
59  
60 <http://pubs.acs.org>.

## References.

- (1) Zhai, Y.; Dou, Y.; Zhao, D.; Fulvio, P. F.; Mayes, R. T.; Dai, S. Carbon Materials for Chemical Capacitive Energy Storage. *Adv. Mater.* **2011**, *23*, 4828–4850.
- (2) Biener, J.; Stadermann, M.; Suss, M.; Worsley, M. A.; Biener, M. M.; Rose, K. A.; Baumann, T. F. Advanced Carbon Aerogels for Energy Applications. *Energy Environ. Sci.* **2011**, *4*, 656–667.
- (3) Wu, Q.; Xu, Y.; Yao, Z.; Liu, A.; Shi, G. Supercapacitors Based on Flexible Graphene/Polyaniline Nanofiber Composite Films. *ACS Nano* **2010**, *4*, 1963–1970.
- (4) Zheng, R.; Gao, J.; Wang, J.; Chen, G. Reversible Temperature Regulation of Electrical and Thermal Conductivity Using Liquid–solid Phase Transitions. *Nat. Commun.* **2011**, *2*, 289.
- (5) Khodadadi, J. M.; Fan, L.; Babaei, H. Thermal Conductivity Enhancement of Nanostructure-based Colloidal Suspensions Utilized as Phase Change Materials for Thermal Energy Storage: A Review. *Renewable Sustainable Energy Rev.* **2013**, *24*, 418–444.
- (6) Kedl, R. J. *Wallboard with Latent Heat Storage for Passive Solar Applications*; Technical Report ORNL/TM-11541; Oak Ridge National Lab: Oak Ridge, 1991.
- (7) Alawadhi, E. M.; Amon, C. H. PCM Thermal Control Unit for Portable Electronic Devices: Experimental and Numerical Studies. *IEEE Trans. Compon. Packag. Technol.* **2003**, *26*, 116–125.

1  
2  
3 (8) Vesligaj, M. J.; Amon, C. H. Transient Thermal Management of Temperature  
4 Fluctuations During Time Varying Workloads on Portable Electronics. *IEEE Trans. Compon.*  
5 *Packag. Technol.* **1999**, *22*, 541–550.  
6  
7

8  
9  
10  
11 (9) Sun, P. C.; Wu, Y. L.; Gao, J. W.; Cheng, G. A.; Chen, G.; Zheng, R. T. Room  
12 Temperature Electrical and Thermal Switching CNT/Hexadecane Composites. *Adv. Mater.* **2013**,  
13 *25*, 4938–4943.  
14  
15  
16

17  
18  
19 (10) Wang, Y.; Tang, B.; Zhang, S. Single-Walled Carbon Nanotube/Phase Change Material  
20 Composites: Sunlight-Driven, Reversible, Form-Stable Phase Transitions for Solar Thermal  
21 Energy Storage. *Adv. Funct. Mater.* **2013**, *23*, 4354–4360.  
22  
23  
24

25  
26  
27 (11) Harish, S.; Ishikawa, K.; Chiashi, S.; Shiomi, J.; Maruyama, S. Anomalous Thermal  
28 Conduction Characteristics of Phase Change Composites with Single-Walled Carbon Nanotube  
29 Inclusions. *J. Phys. Chem. C* **2013**, *117*, 15409–15413.  
30  
31  
32

33  
34  
35 (12) Sanusi, O.; Warzoha, R.; Fleischer, A. S. Energy Storage and Solidification of Paraffin  
36 Phase Change Material Embedded with Graphite Nanofibers. *Int. J. Heat Mass Transfer* **2011**,  
37 *54*, 4429–4436.  
38  
39  
40

41  
42  
43 (13) Chintakrinda, K.; Weinstein, R. D.; Fleischer, A. S. A Direct Comparison of Three  
44 Different Material Enhancement Methods on the Transient Thermal Response of Paraffin Phase  
45 Change Material Exposed to High Heat Fluxes. *Int. J. Therm. Sci.* **2011**, *50*, 1639–1647.  
46  
47  
48

49  
50  
51 (14) Xu, J.-Z.; Chen, T.; Yang, C.-L.; Li, Z.-M.; Mao, Y.-M.; Zeng, B.-Q.; Hsiao, B. S.  
52 Isothermal Crystallization of Poly(l-lactide) Induced by Graphene Nanosheets and Carbon  
53 Nanotubes: A Comparative Study. *Macromolecules* **2010**, *43*, 5000–5008.  
54  
55  
56

1  
2  
3 (15) Li, L.; Li, C. Y.; Ni, C. Polymer Crystallization-Driven, Periodic Patterning on Carbon  
4 Nanotubes. *J. Am. Chem. Soc.* **2006**, *128*, 1692–1699.  
5  
6

7  
8  
9 (16) Yu, A.; Ramesh, P.; Itkis, M. E.; Bekyarova, E.; Haddon, R. C. Graphite  
10 Nanoplatelet–Epoxy Composite Thermal Interface Materials. *J. Phys. Chem. C* **2007**, *111*, 7565–  
11 7569.  
12  
13  
14

15  
16  
17 (17) Yavari, F.; Fard, H. R.; Pashayi, K.; Rafiee, M. A.; Zamiri, A.; Yu, Z.; Ozisik, R.; Borca-  
18 Tasciuc, T.; Koratkar, N. Enhanced Thermal Conductivity in a Nanostructured Phase Change  
19 Composite Due to Low Concentration Graphene Additives. *J. Phys. Chem. C* **2011**, *115*, 8753–  
20 8758.  
21  
22  
23  
24

25  
26  
27 (18) Shahil, K. M. F.; Balandin, A. A. Graphene–Multilayer Graphene Nanocomposites as  
28 Highly Efficient Thermal Interface Materials. *Nano Lett.* **2012**, *12*, 861–867.  
29  
30

31  
32  
33 (19) Yoonessi, M.; Gaier, J. R. Highly Conductive Multifunctional Graphene Polycarbonate  
34 Nanocomposites. *ACS Nano* **2010**, *4*, 7211–7220.  
35  
36

37  
38  
39 (20) Liang, Q.; Yao, X.; Wang, W.; Liu, Y.; Wong, C. P. A Three-Dimensional Vertically  
40 Aligned Functionalized Multilayer Graphene Architecture: An Approach for Graphene-Based  
41 Thermal Interfacial Materials. *ACS Nano* **2011**, *5*, 2392–2401.  
42  
43  
44

45  
46  
47 (21) Walker, L. S.; Marotto, V. R.; Rafiee, M. A.; Koratkar, N.; Corral, E. L. Toughening in  
48 Graphene Ceramic Composites. *ACS Nano* **2011**, *5*, 3182–3190.  
49  
50

51  
52  
53 (22) Deville, S.; Saiz, E.; Nalla, R. K.; Tomsia, A. P. Freezing as a Path to Build Complex  
54 Composites. *Science* **2006**, *311*, 515–518.  
55  
56  
57  
58  
59  
60

1  
2  
3 (23) Elgafy, A.; Lafdi, K. Effect of Carbon Nanofiber Additives on Thermal Behavior of  
4 Phase Change Materials. *Carbon* **2005**, *43*, 3067–3074.  
5  
6

7  
8  
9 (24) Chen, L.; Zou, R.; Xia, W.; Liu, Z.; Shang, Y.; Zhu, J.; Wang, Y.; Lin, J.; Xia, D.; Cao,  
10 A. Electro- and Photodriven Phase Change Composites Based on Wax-Infiltrated Carbon  
11 Nanotube Sponges. *ACS Nano* **2012**, *6*, 10884–10892.  
12  
13  
14

15  
16  
17 (25) Wei, C. Structural Phase Transition of Alkane Molecules in Nanotube Composites. *Phys.*  
18 *Rev. B: Condens. Matter Mater. Phys.* **2007**, *76*, 134104.  
19  
20  
21

22  
23 (26) Yang, J.-S.; Yang, C.-L.; Wang, M.-S.; Chen, B.-D.; Ma, X.-G. Crystallization of Alkane  
24 Melts Induced by Carbon Nanotubes and Graphene Nanosheets: a Molecular Dynamics  
25 Simulation Study. *Phys. Chem. Chem. Phys.* **2011**, *13*, 15476–15482.  
26  
27  
28

29  
30 (27) Babaei, H.; Keblinski, P.; Khodadadi, J. M. Thermal Conductivity Enhancement of  
31 Paraffins by Increasing the Alignment of Molecules through Adding CNT/graphene. *Int. J. Heat*  
32 *Mass Transfer* **2013**, *58*, 209–216.  
33  
34  
35  
36

37  
38 (28) Wilde, G.; Perepezko, J. H. Experimental Study of Particle Incorporation During  
39 Dendritic Solidification. *Mater. Sci. Eng., A* **2000**, *283*, 25–37.  
40  
41  
42

43  
44 (29) Stankovich, S.; Dikin, D. A.; Dommett, G. H. B.; Kohlhaas, K. M.; Zimney, E. J.; Stach,  
45 E. A.; Piner, R. D.; Nguyen, S. T.; Ruoff, R. S. Graphene-based Composite Materials. *Nature*  
46 **2006**, *442*, 282–286.  
47  
48  
49

50  
51 (30) Rampi, M. A.; Whitesides, G. M. A Versatile Experimental Approach for Understanding  
52 Electron Transport through Organic Materials. *Chem. Phys.* **2002**, *281*, 373–391.  
53  
54  
55  
56  
57  
58  
59  
60

1  
2  
3 (31) Hamilton, R. L.; Crosser, O. K. Thermal Conductivity of Heterogeneous Two-  
4 Component Systems. *Ind. Eng. Chem. Fundam.* **1962**, *1*, 187–191.  
5  
6

7  
8  
9 (32) Nan, C.; Birringer, R.; Clarke, D. R.; Gleiter, H. Effective Thermal Conductivity of  
10 Particulate Composites with Interfacial Thermal Resistance. *J. Appl. Phys.* **1997**, *81*, 6692.  
11  
12

13  
14 (33) Minnich, A.; Chen, G. Modified Effective Medium Formulation for the Thermal  
15 Conductivity of Nanocomposites. *Appl. Phys. Lett.* **2007**, *91*, 073105.  
16  
17

18  
19 (34) Ordonez-Miranda, J.; Yang, R.; Alvarado-Gil, J. J. On the Thermal Conductivity of  
20 Particulate Nanocomposites. *Appl. Phys. Lett.* **2011**, *98*, 233111.  
21  
22

23  
24 (35) Nagasaka, Y.; Nagashima, A. Simultaneous Measurement of the Thermal-Conductivity  
25 and the Thermal-Diffusivity of Liquids by the Transient Hot-Wire Method. *Rev. Sci. Instrum.*  
26  
27  
28  
29  
30  
31 **1981**, *52*, 229–232.  
32

33 (36) Huxtable, S. T.; Cahill, D. G.; Shenogin, S.; Xue, L.; Ozisik, R.; Barone, P.; Usrey, M.;  
34 Strano, M. S.; Siddons, G.; Shim, M.; et al. Interfacial Heat Flow in Carbon Nanotube  
35 Suspensions. *Nat. Mater.* **2003**, *2*, 731–734.  
36  
37  
38

39 (37) Shenogin, S.; Xue, L.; Ozisik, R.; Keblinski, P.; Cahill, D. G. Role of Thermal Boundary  
40 Resistance on the Heat Flow in Carbon-nanotube Composites. *J. Appl. Phys.* **2004**, *95*, 8136.  
41  
42  
43

44 (38) Hu, L.; Desai, T.; Keblinski, P. Thermal Transport in Graphene-based Nanocomposite. *J.*  
45  
46  
47  
48  
49  
50  
51 *Appl. Phys.* **2011**, *110*, 033517.  
52  
53  
54  
55  
56  
57  
58  
59  
60

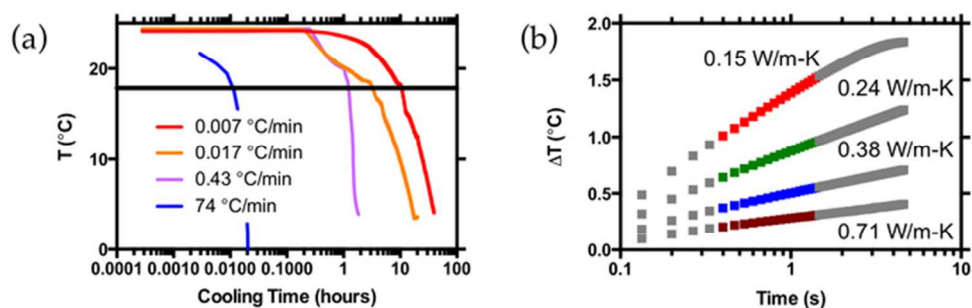


Figure 1. a) Representative plots of sample cooling versus time on a logarithmic scale. The fastest freezing (blue) was liquid nitrogen cooled, while others were frozen with a Peltier cooler. The black line is the phase transition temperature for bulk hexadecane of 17.8 °C. b) Typical transient hot wire thermal conductivity measurement data. The colored region of each line represents the segment of the transient hot wire data used to determine the thermal conductivity. The red, green, blue and brown data points are for liquid hexadecane, liquid nanocomposite, solid hexadecane, and solid nanocomposite, respectively.

60x21mm (300 x 300 DPI)



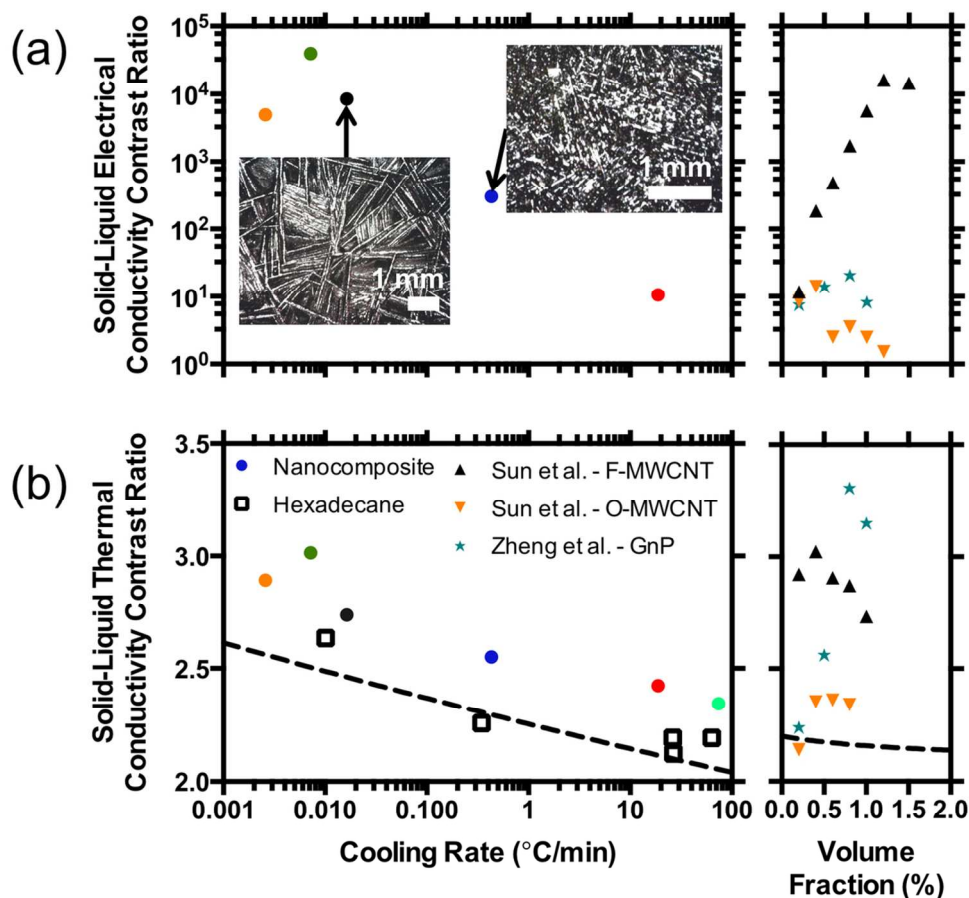


Figure 2. a) The solid-liquid electrical conductivity contrast ratios ( $\sigma_{Solid}/\sigma_{Liquid}$ ) are plotted versus cooling rate for the hexadecane with 1 vol % MLG. The mean liquid state electrical conductivity is 0.02  $\mu\text{S}/\text{cm}$  at 24  $^{\circ}\text{C}$ . Solid measurements were taken at 5  $^{\circ}\text{C}$ . Inset images of the top surface of the nanocomposite were taken with an optical microscope at the respective cooling rates. The length dependence of crystals with cooling rate is notable. To the right are the solid-liquid electrical contrast ratios achieved by Sun *et al.*, and Zheng *et al.* versus volume fraction, as freezing rate was not reported. Sun *et al.* measured suspensions of pristine and anti-agglomeration functionalized multi-walled carbon nanotubes (O-MWCNT and F-MWCNTs) in hexadecane, while Zheng *et al.* measured graphite nanoplatelets (GnP) in hexadecane. b) The solid-liquid thermal conductivity contrast ratios ( $k_{Solid}/k_{Liquid}$ ) are plotted versus cooling rate for bulk hexadecane (black squares) and for hexadecane with 1 vol % MLG (circles color coded by cooling rate). The average liquid state thermal conductivity of the liquid nanocomposite and hexadecane are 0.24 W/m-K and 0.15 W/m-K at 24  $^{\circ}\text{C}$ . The right plot shows the solid-liquid thermal conductivity contrast ratios of Sun *et al.*, and Zheng *et al.* versus vol %. The dashed lines are the Nan *et al.* effective medium predicted contrast ratios (details are in the Methods and Materials section).

107x101mm (300 x 300 DPI)

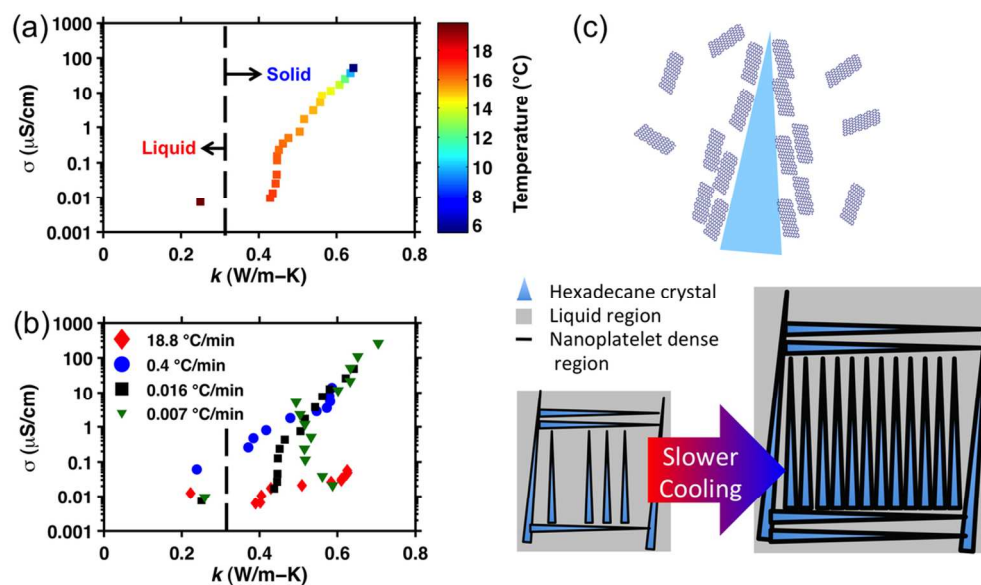


Figure 3. a) Plots the electrical versus thermal conductivity during a freezing at  $0.016\text{ }^\circ\text{C}/\text{min}$  with each datapoints color representing the temperature at that measurement. After freezing there is an exponential increase in electrical conductivity for a linear change in thermal conductivity. b) The trends for electrical versus thermal conductivity taken at various cooling rates show a similar trend except for the rapid liquid nitrogen cooled data ( $19\text{ }^\circ\text{C}/\text{min}$ ). The trend shared by the slowest and moderate cooling rates differ primarily in the final extent of enhancement but not in the path to that enhancement versus temperature. The liquid nitrogen cooled sample ( $19\text{ }^\circ\text{C}/\text{min}$ ) does not follow this trend, and has less improvement in both electrical and thermal conductivity than the slower cooled measurements. c) This graphic illustrates our hypothesis that crystal growth drives MLG nanoplatelets to grain boundary, and that slower freezing will lead to larger hexadecane crystal growth. We suggest that ice-templating leads to increased electrical percolation pathways and reduced electrical resistance between nanoplatelets, as well as reduced inter-nanoparticle thermal resistance.

106x64mm (300 x 300 DPI)

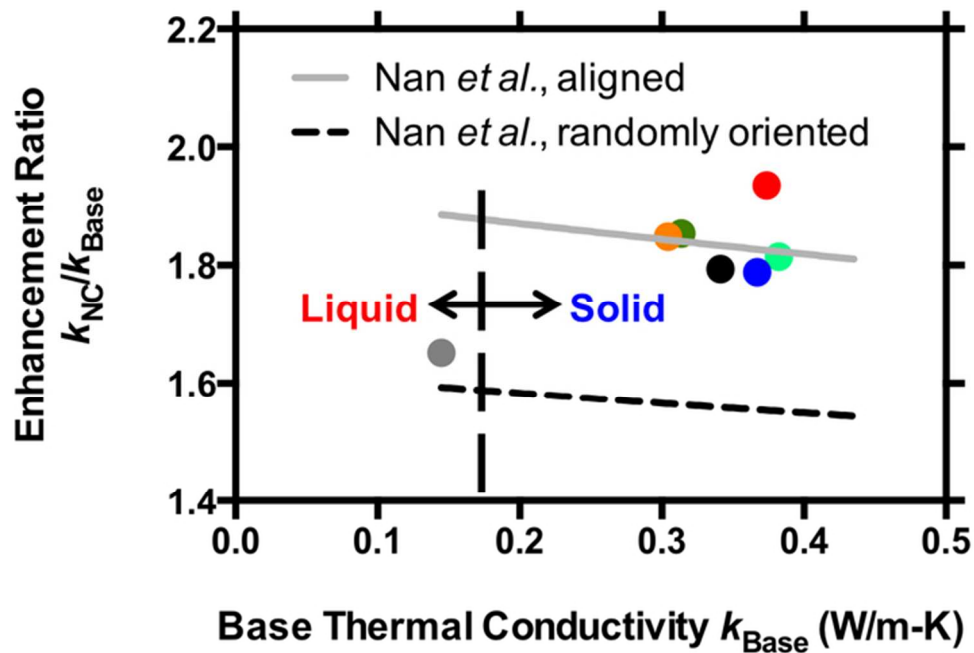


Figure 4. Shows the liquid and solid nanocomposite thermal conductivity enhancements versus base material thermal conductivity. The dashed black line is an effective medium prediction of how enhancement should change versus base thermal conductivity. We used the Nan *et al.* model for oblate ellipsoidal nanoparticles with random (dashed line) and fully aligned (grey line) orientations, with details on the EMT model in Materials and Methods.

62x47mm (300 x 300 DPI)

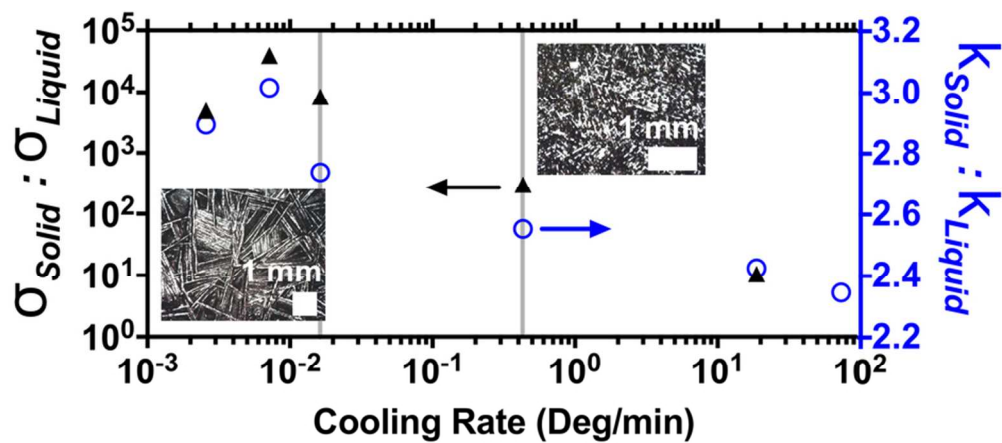


Table of Contents Image  
39x17mm (600 x 600 DPI)